

Available online at www.sciencedirect.com

ScienceDirect

journal homepage: www.elsevier.com/locate/AJPS

Research Article

In situ injectable hydrogel encapsulating Mn/NO-based immune nano-activator for prevention of postoperative tumor recurrence



Shengnan Huang^{a,b}, Chenyang Zhou^b, Chengzhi Song^c, Xiali Zhu^d, Mingsan Miao^a, Chunming Li^{e,*}, Shaofeng Duan^{f,*}, Yurong Hu^{b,*}

^a Academy of Chinese Medical Sciences, Henan University of Chinese Medicine, Zhengzhou 450046, China

^b School of Pharmaceutical Sciences, Henan Key Laboratory of Targeting Therapy and Diagnosis for Critical Diseases, Zhengzhou University, Zhengzhou 450001, China

^c Center for Quantitative Biology, Peking University, Beijing 100871, China

^d School of Pharmaceutical Sciences, Henan University of Chinese Medicine, Zhengzhou 450046, China

^e Department of Pharmacy, Chongqing University Cancer Hospital, Chongqing 400030, China

^f School of Pharmaceutical Sciences, Henan University, Zhengzhou 450046, China

ARTICLE INFO

Article history:

Received 10 July 2023

Revised 24 January 2024

Accepted 5 February 2024

Available online 6 March 2024

Keywords:

Post-surgical tumor recurrence

In situ hydrogel

Immunotherapy

Tumor microenvironment

Manganese (II)

Nitric oxide

ABSTRACT

Postoperative tumor recurrence remains a predominant cause of treatment failure. In this study, we developed an *in situ* injectable hydrogel, termed MPB-NO@DOX + ATRA gel, which was locally formed within the tumor resection cavity. The MPB-NO@DOX + ATRA gel was fabricated by mixing a thrombin solution, a fibrinogen solution containing all-trans retinoic acid (ATRA), and a Mn/NO-based immune nano-activator termed MPB-NO@DOX. ATRA promoted the differentiation of cancer stem cells, inhibited cancer cell migration, and affected the polarization of tumor-associated macrophages. The outer MnO₂ shell disintegrated due to its reaction with glutathione and hydrogen peroxide in the cytoplasm to release Mn²⁺ and produce O₂, resulting in the release of doxorubicin (DOX). The released DOX entered the nucleus and destroyed DNA, and the fragmented DNA cooperated with Mn²⁺ to activate the cGAS-STING pathway and stimulate an anti-tumor immune response. In addition, when MPB-NO@DOX was exposed to 808 nm laser irradiation, the Fe-NO bond was broken to release NO, which downregulated the expression of PD-L1 on the surface of tumor cells and reversed the immunosuppressive tumor microenvironment. In conclusion, the MPB-NO@DOX + ATRA gel exhibited excellent anti-tumor efficacy. The

* Corresponding authors.

E-mail addresses: lchm@cqu.edu.cn (C. Li), sduan@henu.edu.cn (S. Duan), huyr@zzu.edu.cn (Y. Hu).

Peer review under responsibility of Shenyang Pharmaceutical University.

<https://doi.org/10.1016/j.ajps.2024.100901>

1818-0876/© 2024 Published by Elsevier B.V. on behalf of Shenyang Pharmaceutical University. This is an open access article under the CC BY-NC-ND license (<http://creativecommons.org/licenses/by-nc-nd/4.0/>)

results of this study demonstrated the great potential of *in situ* injectable hydrogels in preventing postoperative tumor recurrence.

© 2024 Published by Elsevier B.V. on behalf of Shenyang Pharmaceutical University.

This is an open access article under the CC BY-NC-ND license

(<http://creativecommons.org/licenses/by-nc-nd/4.0/>)

1. Introduction

Surgical resection is an effective and prevalent clinical treatment option for cancer therapy. However, postoperative tumor recurrence and metastasis remain notable clinical challenges [1–3]. The infiltration of local residual tumor cells after surgery and unresectable microscopic tumor foci, especially disseminated cancer stem cells (CSCs) with high tumorigenicity, as well as the invasiveness and the radiotherapy resistance of the remaining tumor cells, are the key factors in postoperative tumor recurrence and metastasis [4–6]. In addition, perioperative trauma-related inflammation and an immunosuppressive microenvironment may promote tumor recurrence by accelerating the growth and dissemination of local tumors [7,8]. Therefore, reversing the immunosuppressive tumor microenvironment (TME) while completely killing residual tumor cells, especially CSCs, is likely an effective strategy to prevent postoperative tumor recurrence.

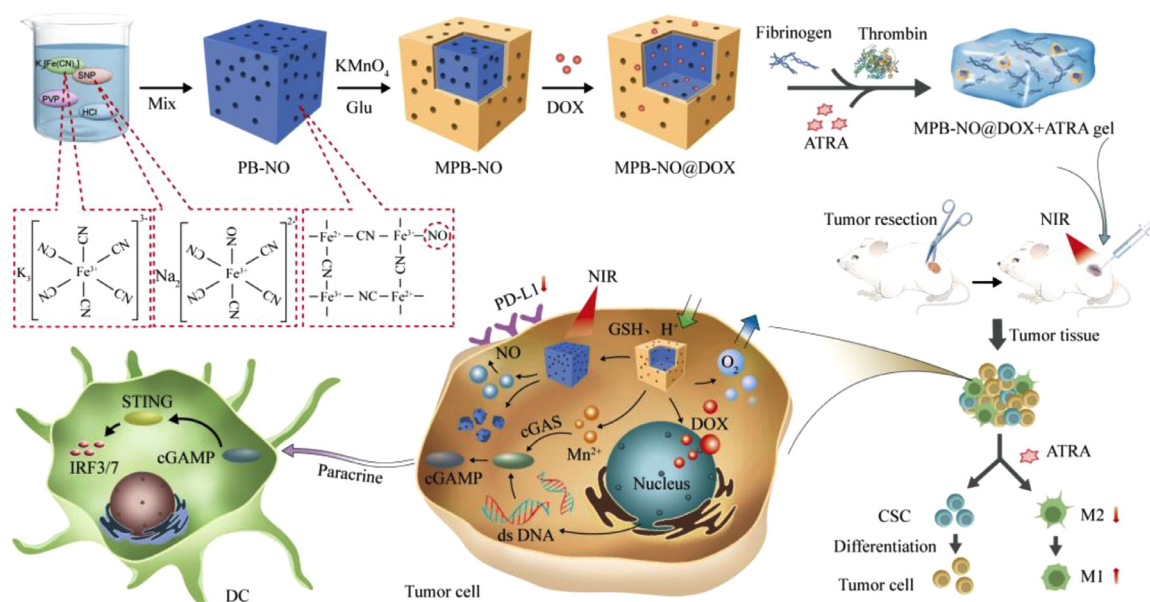
To eliminate the effect of CSCs on tumor recurrence, we propose adopting a differentiation therapy strategy that induces malignant cells into a more mature phenotype using differentiation inducers that are less toxic than conventional chemotherapeutic agents. Differentiation therapy can induce CSCs to lose their malignant proliferation and metastatic properties while increasing their sensitivity to chemotherapy and radiotherapy [9–11]. Recent studies have demonstrated that all-trans retinoic acid (ATRA) can induce CSCs to differentiate into tumor cells in various solid tumors, thereby enhancing their sensitivity to chemotherapy or radiotherapy [12–14]. ATRA could also prevent osteosarcoma cell metastasis, initiation and stemness by inhibiting M2-type tumor-associated macrophages (TAMs) [15,16]. The combination of ATRA-mediated differentiation therapy and chemotherapy via a co-delivery system was demonstrated to be a potent strategy to attenuate the stemness, enhance the cytotoxicity of chemotherapy, and eventually improve the anti-tumor efficacy synergistically [17–19].

Cancer immunotherapy has recently emerged as one of the most promising strategies for tumor treatment and has been proven to be effective against various cancers [20]. Cancer immunotherapy kills tumor cells by promoting multiple stages of the tumor immune cycle, including antigen presentation, T-cell activation, and triggering immune-killing activities [21,22]. Heretofore, a wide range of cancer immunotherapy strategies, such as immune checkpoint inhibitor (ICI) therapy, chimeric antigen receptor (CAR) T-cell therapy, adoptive cell therapy, cancer vaccine and other anti-tumor immunity boosting approaches, have been extensively explored or evaluated in clinical trials. Cancer immunotherapy, applied alone or

in combination with other conventional treatments, such as radiotherapy or chemotherapy, has made remarkable progress [23–25]. Additionally, studies have reported that postoperative immunotherapy can prevent cancer recurrence and metastasis [6,22,26–28]. However, the therapeutic efficacy of immunotherapy still needs to be further improved.

In cancer immunotherapies, activation the innate immune cyclic GMP-AMP synthase-stimulator of interferon genes (cGAS-STING) pathway and its downstream signals promote the overall cancer-immunity cycle by augmenting cross-presentation and immune-killing activity [29–31]. Furthermore, the activation of the cGAS-STING pathway facilitates anti-tumor activity in multiple ways, such as promoting cancer cell senescence, inducing apoptosis, and increasing the protective effect of cytotoxic T cells and natural killer (NK) cell-mediated cytotoxicity [32]. Noteworthy, the cGAS-STING pathway can be activated by Mn^{2+} , thereby activating the host's immune system to promote anti-tumor immunotherapies [33,34]. Mn^{2+} has been demonstrated to improve the sensitivity of cGAS to double-stranded DNA (dsDNA) and enhance STING activity by augmenting the binding affinity of cGAMP-STING [35]. Mn-based nanoparticles (NPs) have been developed as nanocarriers, immunoactivators, and immunomodulators in cancer immunotherapy and have garnered increasing attention [36–38]. Mn-based NPs have many advantages in anti-tumor immunotherapy, including (1) good biocompatibility as drug carrier for delivering immunotherapeutic agents, (2) the ability to regulate the TME by increasing the sensitivity of tumor cells to reactive oxygen species (ROS), through markedly reducing antioxidant and glutathione (GSH) and generating oxygen (O_2) to alleviate the hypoxic TME by reacting with the endogenous hydrogen peroxide (H_2O_2) existing in solid tumors in the acidic TME, thereby enhancing the immunotherapy, and (3) high spin number, long electronic relaxation time, and labile water exchanges when used as a magnetic resonance imaging (MRI) contrast agent for real-time monitoring of tumor response to immunotherapy [39].

As a physiological and pathological messenger, nitric oxide (NO) has been demonstrated to regulate vasodilation, cell proliferation, migration, apoptosis, vascular vasodilation/normalization, and reversion of drug resistance [40,41]. In particular, NO can induce immunogenic cell death (ICD) and ameliorate the immunosuppressive TME by downregulating hypoxia-inducible factor-1 α (HIF-1 α) to relieve hypoxia, restraining the expression of PD-L1 and promoting TAM polarization from the tumor-supportive M2 phenotype to the tumor-restraining M1 phenotype, which is critical for enhancing the anti-tumor effect [42,43]. However, the disadvantages of NO, such as poor stability, short life span, and concentration-dependent biological function have hindered its application in biomedicine [44,45]. Overcoming



Scheme 1 – Schematic illustration of MPB-NO@DOX and therapeutic gel preparation and action mechanism.

these challenges requires the development of stimulus-responsive NO-release systems that release NO on demand to improve anti-tumor efficacy [46].

Since immunotherapy can effectively inhibit tumor metastasis and recurrence, *in situ* immunomodulation is considered safer and more effective than systemic administration. The application of local drug delivery systems at the site of a surgical wound is a favorable approach for post-surgical cancer treatment. Local drug delivery systems, such as wafers, hydrogels, foams, fibers, and micro/nanoparticles, have made tremendous progress [47,48]. As a biodegradable carmustine wafer, Gliadel® is the only clinically approved local implant for post-surgical chemotherapy [49]. However, its treatment efficacy is still unsatisfactory, which may be ascribed to drug resistance, insufficient drug concentration, and an inflammatory reaction in the residual tumor resection in the cavity after surgery [50]. Nevertheless, such solid dosage forms are unsuited for irregular cavities such as the cavity of breast lump after surgery [51,52]. Considering the small and irregular volume of the tumor resection cavity, the *in situ*-forming hydrogel is ideal as a post-surgical implant owing to its three-dimensional network encapsulation ability, excellent malleability, minimally invasive procedure, and shape-adaptive function [53]. Incorporation drug-encapsulated NPs and free drugs in hydrogels is an attractive strategy for preventing burst release, controlling the release profile of the encapsulated drugs, and achieving long-term and effective inhibition of postoperative recurrence [54]. Hydrogels formed *in situ* at postoperative tumor cavities have been shown to inhibit tumor recurrence better than free drugs. Ogunnaike et al. and Chao et al. demonstrated that local implantation of CAR-T cell-loaded hydrogels within the surgical cavity was superior in controlling local tumor growth compared with free CAR-T cells directly inoculated into the tumor resection cavity and conventional intravenous injection of CAR-T cells [55,56]. Besides, hydrogels have extensive application potential in

clinics for purposes other than cancer therapeutics such as tissue regeneration, ocular drug delivery, aesthetic products, and wound healing [57]. Fibrin hydrogels fabricated by thrombin-triggered polymerization of fibrinogen have good biocompatibility and safety and have been approved by the U.S. Food and Drug Administration for application in humans [6,58]. In particular, the postoperative coagulation process could also be accelerated by the fibrin gel to aid in wound healing [59,60]. For instance, Chen et al. fabricated a fibrin hydrogel formed *in situ* for the local delivery of anti-CD47 antibody-loaded CaCO₃ NPs to promote anti-tumor immune responses and inhibit local tumor recurrence and potential metastasis after surgery [6].

In this study, we designed and developed an *in situ* injectable hydrogel, MPB-NO@DOX + ATRA gel, and formed it within the tumor resection cavity by mixing a thrombin solution, a fibrinogen solution containing ATRA, and a Mn/NO-based immune nano-activator termed MPB-NO@DOX to prevent postoperative tumor recurrence (Scheme 1). ATRA released from the gel would not only induce CSC differentiation to reduce the stemness of the tumor but also prevent the TAMs from polarizing into M2-type macrophages. When the tumor site was locally exposed to near-infrared (NIR) laser irradiation, NO was released from the gel because the Fe-NO coordination bond was broken by the heat energy converted from light energy by the NO-doped Prussian blue (PB-NO). The released NO was then able to downregulate PD-L1 expression on the surface of tumor cells, thereby enhancing the immunotherapeutic efficacy of T cells. MnO₂ shell on the surface of PB-NO NPs was taken up by the cells, reduced to Mn²⁺ by GSH, and produced O₂ by catalyzing the decomposition of H₂O₂. Additionally, the generated O₂ could significantly alleviate hypoxic TME and aid in improving the immunosuppressive milieu. The released Mn²⁺ then stimulated the cGAS-STING pathway to boost interferon I (IFN-I) production as an immunological enhancer. Moreover,

the released DOX induced DNA damage in the nucleus, and DNA fragments released into the cytoplasm were captured by cGAS, and cooperated with Mn^{2+} to activate the cGAS-STING pathway and stimulate the anti-tumor immune response.

2. Materials and methods

2.1. Materials

DOX was purchased from Dalian Meilun Biological Technology Co., Ltd. (Liaoning, China). Potassium ferricyanide ($K_3[Fe(CN)_6]$) was purchased from Tianjin Dingsheng Xin Chemical Co. LTD. (Tianjin, China). Potassium permanganate ($KMnO_4$) was purchased from Yantai Shuangshuang Chemical Co., LTD. (Shandong, China). Glucose, polyvinyl pyrrolidone (PVP) and sodium nitroprusside (SNP) were purchased from Shanghai Aladdin Biochemical Technology Co., Ltd. (Shanghai, China). Thrombin was purchased from Hunan Yige Pharmaceutical Co., LTD. (Hunan, China). Fibrinogen was purchased from Yeasen Biotechnology (Shanghai, China) Co., Ltd. (Shanghai, China).

2.2. Cell lines and animals

4T1 cells were obtained from the Key Laboratory of Targeting Therapy and Diagnosis for Critical Diseases in Henan Province. 4T1 were cultured in Roswell Park Memorial Institute-1640 (RPMI-1640) supplemented with 10% fetal bovine serum (FBS) and 1% penicillin-streptomycin at 37 °C in a humidified environment with 5% CO_2 . Female Balb/c mice (6–8 weeks old, 18–20 g) were obtained from Beijing Vital River Laboratory Animal Technology Co., Ltd. (Beijing, China). All procedures were conducted in accordance with the “Laboratory animal–Guideline for ethical review of animal welfare” (China), “Experimental animal management methods of Henan Province” and were approved by the Laboratory Animal Ethics Committee of Henan University of Chinese Medicine.

2.3. Preparation of MPB-NO@DOX

First, PVP-K30 (1.2 g) was dissolved in HCl solution (12 ml, 1 M), followed by the addition of SNP (108 mg) and $K_3[Fe(CN)_6]$ (120 mg). Then, the solution was stirred in the dark until it became clear and transparent, and heated at 80 °C for 12 h. After that, the resulting mixture was centrifuged at 10,000 rpm for 15 min, and washed with ddH_2O three times to obtain PB-NO.

Glucose (60 mg) and PVP (50 mg) were dissolved in ddH_2O (8 ml), followed by the addition of a solution of PB-NO NPs (10 mg) dissolved in ddH_2O (2 ml). After the solution was stirred for 10 min, 6.25 mg $KMnO_4$ was added and the reaction proceeded for 1 h. Next, the resulting mixture was centrifuged at 10,000 rpm for 8 min to obtain MPB-NO NPs. Then, MPB-NO NPs (6 mg) and DOX (3 mg) were dissolved in ddH_2O (5 ml) and stirred in the dark for 12 h, and the solution was centrifuged at 10,000 rpm for 15 min to obtain MPB-NO@DOX NPs. The supernatant was collected and its absorbance at 480 nm was measured with a UV spectrophotometer

to calculate the encapsulation rate and drug loading rate.

2.4. Preparation of therapeutic gel

According to our group's previous research, 10 mg/ml fibrinogen solution and 50 U/ml thrombin solution were selected to prepare fibrin gel. The specific experimental steps were as follows: (1) preparation of fibrinogen solution: fibrinogen was dissolved with 0.9% normal saline at 37 °C and filtered by 0.22 μm filter membrane to prepare fibrinogen solution at a concentration of 10 mg/ml; (2) preparation of thrombin solution: 40 mM $CaCl_2$ solution was prepared and filter with 0.22 μm membrane for sterilization to prepare thrombin solution at a concentration of 50 U/ml. (3) fibrin gel was prepared by mixing fibrinogen solution and thrombin solution at a volume ratio of 1:2, followed by incubation at 37 °C for 15 min. Preparation of postoperative therapeutic gel: MPB-NO@DOX and ATRA were added into the fibrinogen solution under stirring, and then mixed with thrombin solution as mentioned above to prepare MPB-NO@DOX + ARTA gel.

2.5. Catalase activity of PB-NO and MPB-NO

Appropriate concentrations of PB-NO and MPB-NO NPs were prepared respectively, and PBS was used as blank control. An equal amount of H_2O_2 solution was added to the above three solutions respectively, and then the absorbance at 240 nm was measured by UV and the decomposition rate of H_2O_2 catalyzed by different nanoparticles was calculated according to the H_2O_2 standard curve. In addition, the catalase activity of the nanoparticles was further determined by the concentration of dissolved O_2 in the solution, which was detected by the dissolved oxygen electrode of the multi-parameter analyzer. Since PB-NO had a good photothermal conversion effect, the above groups were compared with laser irradiation to study the effect of light on the catalase activity.

2.6. DOX and Mn^{2+} release in vitro

The DOX release from MPB-NO@DOX *in vitro* was detected by the dialysis method in this study. Briefly, MPB-NO@DOX was dispersed in deionized water and placed in a dialysis bag (MWCO = 3,500 Da), and then immersed in different PBS media (pH 7.4, pH 6.4, pH 5.0, pH 7.4 + $C_{GSH} = 2.5$ mM, pH 7.4 + $C_{GSH} = 5$ mM, pH 7.4 + $C_{GSH} = 10$ mM, pH 5.0 + $C_{GSH} = 10$ mM, pH 5.0 + $C_{GSH} = 10$ mM + NIR) in a thermostatic oscillator at 120 rpm and 37 °C in the dark. 2 ml of release medium was taken out at 0.5, 1, 2, 4, 6, 8, 12 and 24 h, respectively, and the same amount of fresh PBS was added immediately. The DOX content was determined by a fluorescence spectrophotometer (RF-5301 PC, SHIMADZU) and the amount of released DOX was calculated according to the following equation. In addition, to study the effect of laser irradiation on drug release, MPB-NO@DOX was irradiated with an 808 nm laser (1 W/cm², 5 min) before each sampling.

$$\text{Cumulative release(\%)} = \left(C_n \times \sum_{i=1}^{n-1} C_i \times V_0 \right) / m \times 100\%$$

Where C_n was the drug concentration in the release medium at a certain time point, V was the total volume of the release medium, C_i was the drug concentration in the release medium at the sampling point, V_0 was the volume of each sample, and m was the total amount of drugs in the nanoparticle.

To detect the release of Mn^{2+} from MPB-NO, an MPB-NO stock solution at a concentration of 1 mg/ml in PBS was prepared. Then, 1 ml of stock solution was added to 2 ml 30% nitric acid, boiled for 15 min, and then centrifuged at 12,000 rpm for 10 min. The supernatant was collected and the content of Mn^{2+} was determined by ICP-MS. MPB-NO stock solutions at a concentration of 1 mg/ml in PBS at pH 7.4, pH 5.0, and pH 5.0 + GSH (5 mM) were prepared, respectively. Then, 1 ml of each solution was incubated on a shaker at 37 °C for 1 h, and then centrifuged at 12,000 rpm for 10 min. The supernatant was then collected and the content of Mn^{2+} was determined by ICP-MS.

2.7. Gel degradation, ATRA and MPB-NO@DOX release from gel

We transferred the prepared gel to 12-well plates, and added PBS containing 10% FBS to the 12-well plates. Then, the degradation rate of the gel was estimated by measuring the concentration of fibrin in the supernatants using a UV-vis-NIR spectrophotometer on 0, 1, 2, 3, 4, 5 and 6 d, respectively. The therapeutic gel was infiltrated in PBS (pH 6.4) containing 10% FBS. For a total of 6 d, 2 ml of release medium was taken daily and the same amount of fresh medium was immediately added. The absorbance of ATRA was then measured by UV, and its release was calculated according to its standard curve. At the same time, TEM was used to determine the particle size of MPB-NO@DOX in the release medium to investigate whether their morphology changed.

2.8. Photothermal conversion effect in vitro

MPB-NO water solutions (1 ml) with concentrations of 0, 0.1, 0.2, 0.5 and 1.0 mg/ml were added to quartz cells respectively, and then irradiated by an 808 nm laser with a power density of 1.0 W/cm² for 5 min. Meanwhile, MPB-NO at 0.1 mg/ml was irradiated for 5 min by an 808 nm laser with the power density of 0.5, 1.0, 1.5, 2.0 and 2.5 W/cm² respectively. An infrared thermal imager (Ti-200, Fluke) was used to record the temperature changes during the irradiation. Meanwhile, the photothermal conversion stability of MPB-NO was evaluated by five ON/OFF cyclic irradiation tests. The MPB-NO aqueous solution was first irradiated with an 808 nm laser for 5 min, then the laser was turned off and the solution was allowed to cool to room temperature naturally. This operation was repeated 5 times. An infrared thermal imager was used to record the temperature changes during the whole process.

2.9. Cellular uptake in vitro

4T1 cells were seeded on a 12-well plate at a density of 1×10^5 cells/well and incubated for 24 h, followed by the addition of free DOX or MPB-NO@DOX. After incubation for 2 h, 4 h,

6 h and 8 h, the medium was discarded and the cells were washed 3 times with PBS buffer, followed by the addition of 500 μ l 4% paraformaldehyde (PFA) and incubation for 15 min. Then, the cells were washed 3 times with PBS buffer to remove PFA, followed by the addition of 500 μ l DAPI to stain the nuclei. After 15 min, the cells were washed again with PBS buffer and placed under a fluorescence microscope (Nikon Eclipse 80i, Nikon) to observe the uptake of free DOX or MPB-NO@DOX. The cells co-cultured free DOX or MPB-NO@DOX were collected and detected by a flow cytometer (FACS Calibur, BD Biosciences).

2.10. NO release from MPB-NO in vitro

4T1 cells were seeded at a density of 1×10^5 cells/well into 12-well plates containing cell crawlers and incubated in a cell culture incubator for 24 h. The cell culture dishes were cultured with fresh culture medium containing PB, PB-NO, and MPB-NO, respectively. After incubation for 8 h, the dishes were washed three times with PBS, and incubated with the DAF-FM DA fluorescent probe dilution at 5 μ M for 20 min before being washed three times with PBS and fresh culture medium was added. To investigate the effect of the NIR laser irradiation on NO release in vitro, the cells were exposed to an 808 nm laser at a power density of 2.0 W/cm² for 5 min. The cells were then fixed in 4% PFA for 20 min at 37 °C. After washing three times with PBS buffer to remove the PFA, 700 μ l Hoechst staining solution was added to each well for 15 min, and the cells were washed three times with PBS buffer. The crawling slices were selected and examined under a fluorescence microscope to determine NO release. In addition, the cells were collected and detected by a flow cytometer.

2.11. PD-L1 expression in vitro

We used Western blotting to detect PD-L1 protein expression of the cells under hypoxic conditions with various treatments. Logarithmic growth phase cells were inoculated in cell culture dishes, and when the cell density reached 70%, a complete medium containing 100 μ M cobalt chloride (CoCl₂) and 200 μ g/ml MPB-NO was added to continue the culture, and the cells were irradiated with an 808 nm laser (2.0 W/cm², 5 min) after culture for 8 h. After 24 h, the medium was discarded, and the cells were washed twice with 2 ml of pre-cooled PBS, digested with trypsin, and collected. Each cell sample was mixed with 150 μ l RIPA lysate and lysed on ice for 30–60 min. After centrifuging the fully lysed samples at 4 °C at 14,000 rpm for 5 min, the supernatant was aspirated and quantified using the BCA protein kit. The expression of PD-L1 protein in cell extracts was determined using Western blotting.

2.12. Migration assay

4T1 cells were seeded on a 6-well plate with a density of 2×10^5 cells/well. When the cells grew up to 80%–90%, two scratches were made perpendicular to the bottom of the plate, followed by the addition of a culture medium containing different concentrations of ATRA. Images were then taken under the microscope at 0 and 24 h respectively and the relative migration width was calculated.

2.13. Optimization of Mn and DOX concentrations for activation of the cGAS-STING pathway

The optimal concentrations and ratios of Mn^{2+} and DOX required for activation of the cGAS-STING pathway were determined by co-culturing 4T1 and DC 2.4 cells and treating them with DOX and Mn^{2+} at different concentrations. 4T1 and DC 2.4 cells were inoculated on cell culture dishes at a ratio of DC 2.4: 4T1 = 5: 1 and treated with media containing DOX and $MnCl_2$ at various concentrations for 8 h. After being digested, the cells were collected, mixed with the RIPA lysis solution, and lysed on ice for 1 h. The lysed samples were then centrifuged at 14,000 rpm for 5 min at 4 °C, and the supernatant was collected for the protein concentrations determination by BCA. The target proteins STING and pIRF3 were assessed by Western blotting assay. When the DOX concentration was 2 µg/ml, $MnCl_2$ concentrations at 0.1, 0.2, 0.3, 0.4, 0.5 and 0.6 mM were determined. After determining the optimal Mn^{2+} concentration, the Mn^{2+} concentration was fixed and the appropriate DOX concentrations were screened. The DOX concentrations were 0.157, 0.313, 0.625, 1.25, 2.5 and 5 µg/ml, respectively.

2.14. Antitumor efficacy in vivo

BALB/c mice were inoculated with 2×10^6 4T1 cells in the right flanks. When the tumor volume reached about 500 mm³, the mice were randomly divided into eight groups with six mice in each group: NS gel, PB gel, MPB-NO NPs gel, MPB-NO NPs gel + NIR, MPB-NO@DOX NPs gel, MPB-NO@DOX NPs gel + NIR, MPB-NO@DOX NPs + ATRA gel, MPB-NO@DOX NPs + ATRA gel + NIR. To establish the postoperative tumor model, a surgical resection cavity was made by removing roughly 90% of the engrafted tumor after tumor inoculation for 12 d. Various fibrin gels encapsulating different nanoparticles were injected into the surgical tumor cavity immediately, and the wound was then sutured with the Autoclip wound clip system. An 808 nm laser irradiation (1.0 W/cm², 3 min) was given once every 2 d for a total of 7 times. During this time, the temperature of the tumor site was recorded using infrared thermography to investigate the photothermal conversion ability of MPB-NO *in vivo*. The change of tumor volume was measured before each laser irradiation, and the curve of tumor volume with time was plotted. After the treatments, the mice were euthanized, the tumor tissues were dissected and removed, weighed, placed in 4% PFA solution for 24 h, paraffin-embedded, sectioned, and prepared, stained using hematoxylin-eosin (H&E) (Servicebio, cat. no. G1005) and TUNEL assay kit (Servicebio, cat. no. GDP1042) in accordance with the manufacturer's protocol, and placed under a light microscope for observation.

2.15. Western blotting analysis

Total proteins were first extracted from cells or tumor tissue and quantitated by BCA. The samples were loaded, separated by gel electrophoresis, transferred to the PVDF membranes, and then primary antibody including STING (Cell Signaling, cat. no. 13647S), pIRF3 (Cell Signaling, cat. no. 29047S) and PD-L1 (D4H1Z) (Cell Signaling, cat. no. 60475S)

at 4 °C overnight. Then, the PVDF membranes were further incubated with HRP-labeled Goat Anti-Rabbit IgG (Beyotime, cat. no. A0208) and then placed into an automatic fluorescence chemiluminescence imaging system BeyoECL Plus (Beyotime, cat. no. P0018S) for exposure imaging.

2.16. Immunohistochemical staining (IHC) assay

Paraffin-embedded tumor tissues were sectioned, treated with anti-SOX2 Rabbit pAb (Servicebio, cat. no. GB11249) and anti-Nanog Rabbit pAb (Servicebio, cat. no. GB11331), and then stained with IgG antibody that was labeled with horseradish peroxidase to examine the distribution of CSCs in tumor tissues using a microscope.

2.17. Toxicity examination in vivo

After the establishment of a postoperative tumor model, the body weight of the mice was recorded during the treatments to evaluate the safety of the therapeutic gel. After the treatments, the mice were euthanized to collect major tissues including the heart, liver, spleen, lung, and kidney. The slices were stained with H&E staining solution, sealed, and observed under a microscope to further evaluate the toxicity *in vivo*. After the treatments, blood was collected into centrifuge tubes containing sodium heparin for analysis using a standard blood test. In addition, blood was collected in EP tubes and then allowed to stratify at ambient temperature before being centrifuged at 3,000 rpm for 10 min. The supernatant was collected and the blood biochemical indicators were tested using a completely automated blood biochemistry analyzer.

2.18. Statistical analysis

Data were expressed as mean ± standard deviation by GraphPad Prism 9 software. The data underwent statistical examination utilizing Student's t-test and the analysis of variance (ANOVA). P-Values less than 0.05 were considered statistically significant (* $P < 0.05$, ** $P < 0.01$, *** $P < 0.001$, and **** $P < 0.0001$).

3. Results and discussion

3.1. Preparation and characterization of MPB-NO@DOX

PB-NO was synthesized as previously reported [61]. The size of the PB-NO NPs was controlled by changing the acidity and mass of the reactants (Table S1), and finally, PB-NO with 129 nm was selected for subsequent experiments (Fig. S1). A strong stretching vibration of the C≡N group at 2086 cm⁻¹ was observed in the FTIR spectra of PB and PB-NO, while an infrared peak of N=O vibration at 1944 cm⁻¹ was only observed in PB-NO, which proved the successful incorporation of sodium nitroprusside (SNP) into the Prussian blue (PB) lattice (Fig. S2). The hydration particle size and zeta potential of PB-NO were 130.57 ± 3.39 nm and -25.73 ± 1.64 mV, respectively. Mn-containing PB-NO (MPB-NO) was obtained by depositing MnO_2 onto the surface of PB-NO. The hydrodynamic size of MPB-NO increased by

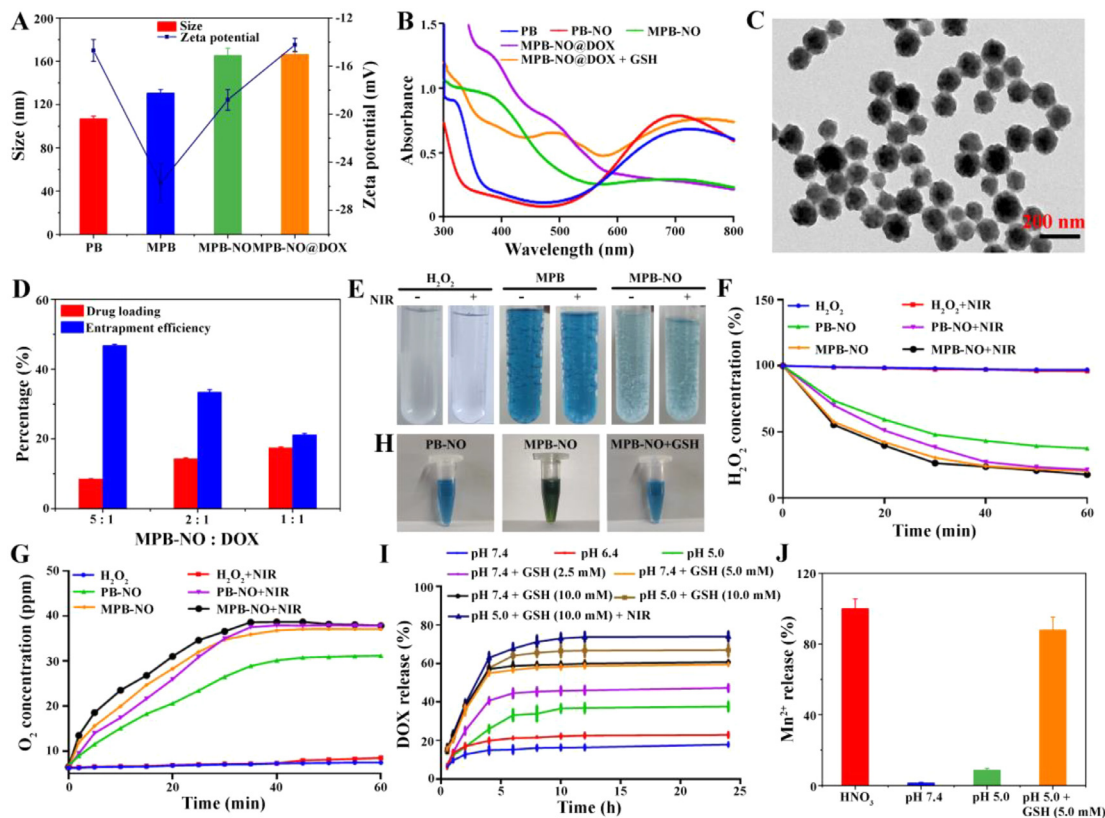


Fig. 1 – Therapeutic illustration of fibrin gel and characterization of MPB-NO@DOX. (A) Hydration particle size (column) and zeta potential (line) of PB, PB-NO, MPB-NO and MPB-NO@DOX. (B) Ultraviolet-visible-NIR spectra of PB, PB-NO, MPB-NO and MPB-NO@DOX. (C) TEM image of MPB-NO@DOX. (D) Drug loading and encapsulation rate of MPB-NO under different conditions (MPB-NO:DOX = 5:1, 2:1 and 1:1, w/w). (E) PB-NO and MPB-NO catalyzed H_2O_2 to produce O_2 . (F) Catalase activities of PB-NO and MPB-NO were investigated by detecting the decomposition of H_2O_2 . (G) Catalase activities of PB-NO and MPB-NO were investigated by detecting O_2 generation. (H) The redox reaction between MPB-NO and GSH. The solution turned blue after the decomposition of MnO_2 . (I) DOX released from MPB-NO@DOX at different pH values (7.4, 6.4 and 5.0) and concentrations of GSH (2.5, 5.0, and 10 mM) upon NIR irradiation at a power density of 2.0 W/cm^2 for 5 min. (J) Mn^{2+} released from MPB-NO at different pH values (7.4 and 5.0) and in the presence of GSH (5 mM).

30 nm correspondingly in comparison with PB-NO, and the potential of -18.80 ± 0.86 mV was primarily represented by the zeta potential of MnO_2 (Fig. 1A). In addition, the characteristic absorption peak of MnO_2 at 380 nm was observed in the UV spectrum of MPB-NO, further confirming the successful deposition of MnO_2 onto the surface of PB-NO (Fig. 1B). The XRD patterns of PB-NO and MPB-NO revealed the same diffraction peaks as those of PB, indicating that the embedded SNP and the MnO_2 shell layer on the surface had no effect on the crystal structure of PB (Fig. S3). Finally, DOX was loaded into MPB-NO via electrostatic adsorption and coordination bonds to obtain DOX-loaded MPB-NO (MPB-NO@DOX), resulting in the zeta potential of -14.23 ± 0.54 mV (Fig. 1A). The transmission electron microscopy (TEM) results indicated that the particle size of MPB-NO@DOX was approximately 100 nm (Fig. 1C). Different mass ratios of MPB-NO to DOX (5:1, 2:1, and 1:1) were prepared, and the optimal ratio was selected according to the drug loading and encapsulation rate. The amount of loaded DOX increased with a decrease in the carrier-to-drug

mass ratio, but the encapsulation rate decreased (Fig. 1D). After careful consideration, MPB-NO:DOX = 2:1 (w/w) was selected for subsequent experiments. According to the UV spectrum results, PB-NO and PB had similar absorption peaks at approximately 700 nm, which were due to electron transfer between Fe (II) and Fe (III) in the structures of PB and PB-NO (Fig. 1B). Importantly, MPB-NO@DOX exhibited a shoulder slit at 480 nm, confirming that DOX was successfully loaded into MPB-NO. Due to the responsiveness of MnO_2 to GSH, 5 mM GSH was added to the MPB-NO@DOX solution to validate this property. The characteristic peaks of DOX and PB-NO at 480 nm and 700 nm appeared respectively, while that of MnO_2 at 380 nm disappeared in the presence of GSH, suggesting that MnO_2 reacted with GSH and collapsed (Fig. 1B). To further investigate the redox ability of MPB-NO, 5 mM GSH was added to the MPB-NO solution. The dark green solution turned blue, indicating that the MnO_2 encapsulated in the outer layer rapidly decomposed in the presence of GSH (Fig. 1H). As evident from Fig. 1E-I, both PB-NO and MPB-NO exhibited catalase (CAT)-like activity, and the activity of

MPB-NO was significantly higher than that of PB-NO within 30 min, which might be because MnO_2 underwent a redox reaction with H_2O_2 and accelerated the decomposition rate of H_2O_2 . In addition, the CAT-like activities of PB-NO and MPB-NO enhanced with laser irradiation, as indicated by a slight increase in the catalytic decomposition rate and final catalytic decomposition amount of PB-NO.

The drug release curves of MPB-NO@DOX revealed that only 17.9% of DOX was released after 24 h at pH 7.4, while this increased to 23.0% and 37.7% at pH 6.4 and 5.0, respectively (Fig. 1). This may be attributed to the decreased coordination capacity of DOX and Mn^{2+} under acidic conditions. Next, different concentrations of GSH were used to examine the responsiveness of MPB-NO@DOX to GSH at pH 7.4. The percentages of cumulative DOX release after 24 h from MPB-NO@DOX in the presence of GSH at concentrations of 2.5, 5 and 10 mM were 47.3%, 59.5% and 60.8% (after 24 h), respectively, indicating that MPB-NO@DOX demonstrated good release performance in the presence of GSH, and the response capacity was proportional to the concentration of GSH. At pH 5.0 and with 10 mM GSH, the percentage of cumulative DOX release after 24 h reached 67.1% and further increased to 74.1% with laser irradiation. This enhanced drug release might be due to the good photothermal conversion effect of MPB-NO, which accelerated the movement of small drug molecules after heat generation.

The *in vitro* release capacity of Mn^{2+} from the MPB-NO was also determined. The total content of Mn^{2+} released from MPB-NO was 139.0 mg/l after digestion with dilute nitric acid (Fig. 1). The concentration and the release rate of Mn^{2+} released at pH 7.4 was only 1.888 mg/l and 1.358%, respectively, while these values increased to 8.648 mg/l and 6.221%, respectively, at pH 5.0. At pH 5.0 and with 5 mM GSH, the concentration, and the release rate of Mn^{2+} were as high as 122.1 mg/l and 87.87%, respectively, suggesting that a large amount of Mn^{2+} was released from MPB-NO in the presence of GSH and an acidic microenvironment.

3.2. Photothermal conversion property of MPB-NO@DOX and characterization of MPB-NO@DOX + ATRA gel

The results of the rheological test demonstrated a gel-like behavior of the MPB-NO gel and an ultrafast sol-gel transition of the mixture of fibrinogen solution containing MPB-NO and thrombin solution (Fig. S4). As depicted in Fig. 2A, the MPB-NO@DOX- and ATRA-co-loaded gel, MPB-NO@DOX + ATRA gel, exhibited a porous honeycomb network structure with uniform pore sizes. The degradation rate of the gel in RPMI 1640 medium and the release curve of ATRA from the gel demonstrated that ATRA could be released continuously for 6 d with a maximum release rate of 95.78% (Fig. 2B and 2C). The TEM image of MPB-NO@DOX released from the gel showed that the size and dispersion of MPB-NO@DOX did not change significantly (Fig. 2D), indicating that the gel had a limited effect on the properties of MPB-NO@DOX. As presented in Fig. 2E and F, MPB-NO had a high photothermal conversion effect *in vitro*, which was positively correlated with the concentration of MPB-NO and irradiation power density. In addition, MPB-NO exhibited good photothermal conversion stability (Fig. 2G).

3.3. Cell viability

As a broad-spectrum anti-tumor drug, DOX can kill tumor cells by inserting into DNA, inhibiting DNA synthesis, triggering ICD, and activating the immune response [62–64]. To ensure that the DOX concentration would not affect cell viability in subsequent experiments, the cytotoxicity of DOX to 4T1 and RAW 264.7 cells investigated. The survival rates of 4T1 and RAW 264.7 cells at DOX concentration of 2.5 $\mu\text{g}/\text{ml}$ were 89.9% and 87.7%, respectively (Fig. S5). Accordingly, we chose the DOX concentration of 2.5 $\mu\text{g}/\text{ml}$ for the subsequent experiments.

To ensure that the drug vectors, including PB-NO and MPB-NO, did not affect 4T1 cells in subsequent experiments, we investigated their cytotoxicity. The cell viability reached 94% even when the concentrations of PB-NO and MPB-NO were as high as 200 $\mu\text{g}/\text{ml}$ (Fig. S6). No obvious toxicity was observed in 4T1 cells when the concentrations of PB-NO and MPB-NO were less than 200 $\mu\text{g}/\text{ml}$. Consequently, PB-NO and MPB-NO could be used as safe drug carriers in subsequent studies.

We intended to use ATRA to inhibit and reverse the effect of macrophage polarization on the M2-type TAM in the TME. To that end, we investigated the effect of ATRA at concentrations of 0.25, 0.5, 1, 2.5, 5, 7.5, and 10 μM on the viability of RAW 264.7 cells, to ensure that ATRA was not toxic to macrophages. The viability of RAW 264.7 cells was above 90% when the ATRA concentration was less than 5 μM , although it decreased to 87.24% with 7.5 μM ATRA (Fig. S7). Therefore, the maximum safe concentration of ATRA was 5 μM for RAW 264.7 cells, so it was used in the subsequent experiments.

To examine the effect of the MPB-NO@DOX + ATRA gel on cell viability, we first co-cultured 4T1 or HUVEC cells with NS gel or MPB-NO@DOX + ATRA gel extracts for 1–6 d and then detected cell viability. The toxicity of the NS gel was negligible, and cell viability increased with increasing extraction time of the blank gel. The 4T1 and HUVEC cell viabilities following incubation with the NS gel extracts for 6 d were 105.19% and 103.19%, respectively (Fig. S8). We hypothesized that this was because of the weak effect of fibrin on the promotion of cell growth. The 4T1 cell viabilities after co-culturation with MPB-NO@DOX + ATRA gel extracts for one and 2 d were 84.80% and 85.6% respectively. However, the 4T1 cell viability reached 94.22% after co-culturation with MPB-NO@DOX + ATRA gel extracts for 6 d. We speculated that this was because the drug in the gel was released slightly more rapidly in the first 2 d, and the drug concentration was slightly higher than the safe concentration. These results demonstrated the good biocompatibility of MPB-NO@DOX + ATRA gel.

3.4. Cellular uptake

As depicted in Fig. 3A, DOX partially entered the nucleus in the free DOX group at 4 h, whereas almost no DOX entered the nucleus in the MPB-NO@DOX group. At 6 h, most DOX in the free DOX group entered the nucleus, whereas only a portion of DOX in the MPB-NO@DOX group entered the nucleus. At 8 h, most DOX in the MPB-NO@DOX and DOX groups was localized to the nucleus. A possible reason for the different rates of DOX entry into the nucleus was that free DOX could directly enter the nucleus through the nuclear pore after being ingested

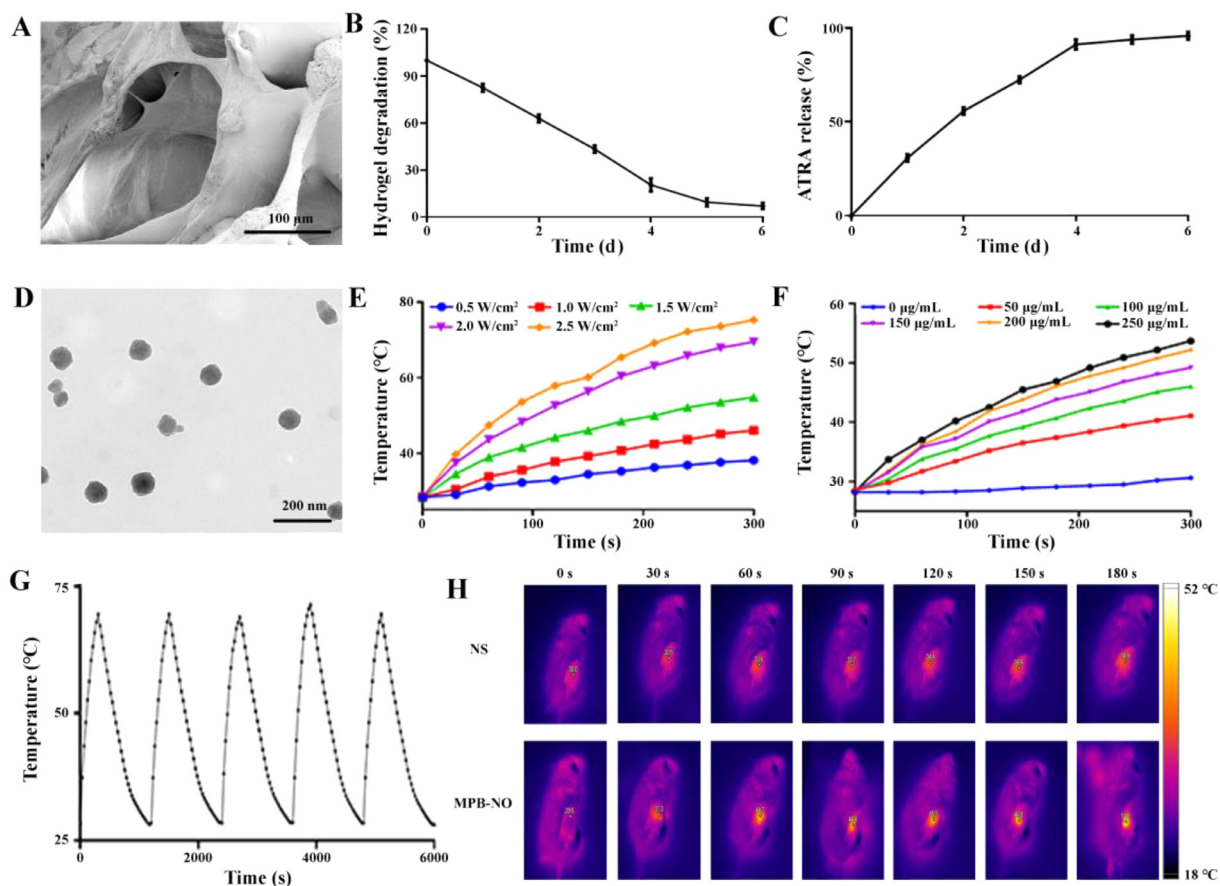


Fig. 2 – Characteristics of MPB-NO@DOX and MPB-NO@DOX + ATRA gel. (A) SEM image of fibrin gel loaded with MPB-NO@DOX and ATRA. The scale bar was 100 µm. **(B)** The degradation rate of the fibrin gel in medium RPMI 1640. **(C)** ATRA released from the gel. **(D)** TEM image of MPB-NO@DOX released from the gel. The scale bar was 200 nm. **(E)** Photothermal conversion curves of MPB-NO@DOX at 100 µg/ml under 808 nm laser irradiation at different power densities (0.5, 1.0, 1.5, 2.0, and 2.5 W/cm²) for 5 min. **(F)** Photothermal conversion curves MPB-NO@DOX at different concentrations (0, 50, 100, 150, and 200 µg/ml) under 808 nm laser irradiation at the power density of 1.0 W/cm² for 5 min. **(G)** Photothermal conversion stability experiment of MPB-NO@DOX tested by five ON/OFF circles. **(H)** Infrared thermography photos of the mice injected with the gel loaded with NS and MPB-NO@DOX upon 808 nm laser irradiation at the power density of 1.5 W/cm² for 6 min.

by the cells, whereas MPB-NO@DOX could not directly enter the nucleus owing to its larger particle size, and DOX had to be released from MPB-NO@DOX. Most of the DOX was released from MPB-NO@DOX after 4–6 h in response to GSH and the weakly acidic TME. This substantiated our hypothesis that DOX required a longer time to enter the nucleus in the MPB-NO@DOX group than in the free DOX group because DOX was required to be released from MPB-NO@DOX. Our flow cytometry results further confirmed this hypothesis (Fig. S9).

3.5. NO release in MPB-NO and expression of PD-L1 in vitro

4-Amino-5-methylamino-2',7'-difluorofluorescein diacetate (DAF-FM DA) is cell-permeable and can be catalyzed by esterase in the cell to form DAF-FM, which cannot cross

the cell membrane. DAF-FM exhibits weak fluorescence but can produce stronger green fluorescence after reacting with NO. Therefore, DAF-FM DA can be used as a probe to detect cellular NO levels. As evident from Fig. 3B, except for the MPB-NO + NIR group, no obvious green fluorescence was observed in NIR, PB + NIR, or MPB-NO groups, indicating that NO was released from MPB-NO only when the cells were exposed to 808 nm laser irradiation. This can be attributed to the destruction of the Fe-NO bond in the MPB-NO structure by laser irradiation.

Studies have demonstrated that NO can reduce PD-L1 expression by inhibiting HIF-1 α expression [65]. In this study, 4T1 cells were cultured in a medium containing CoCl₂ to simulate the hypoxic TME, and PD-L1 expression was detected by western blotting. As depicted in Fig. 3C, PD-L1 expression in the hypoxic group was much higher than that in the 20% O₂ group, and PD-L1 expression was significantly lower in

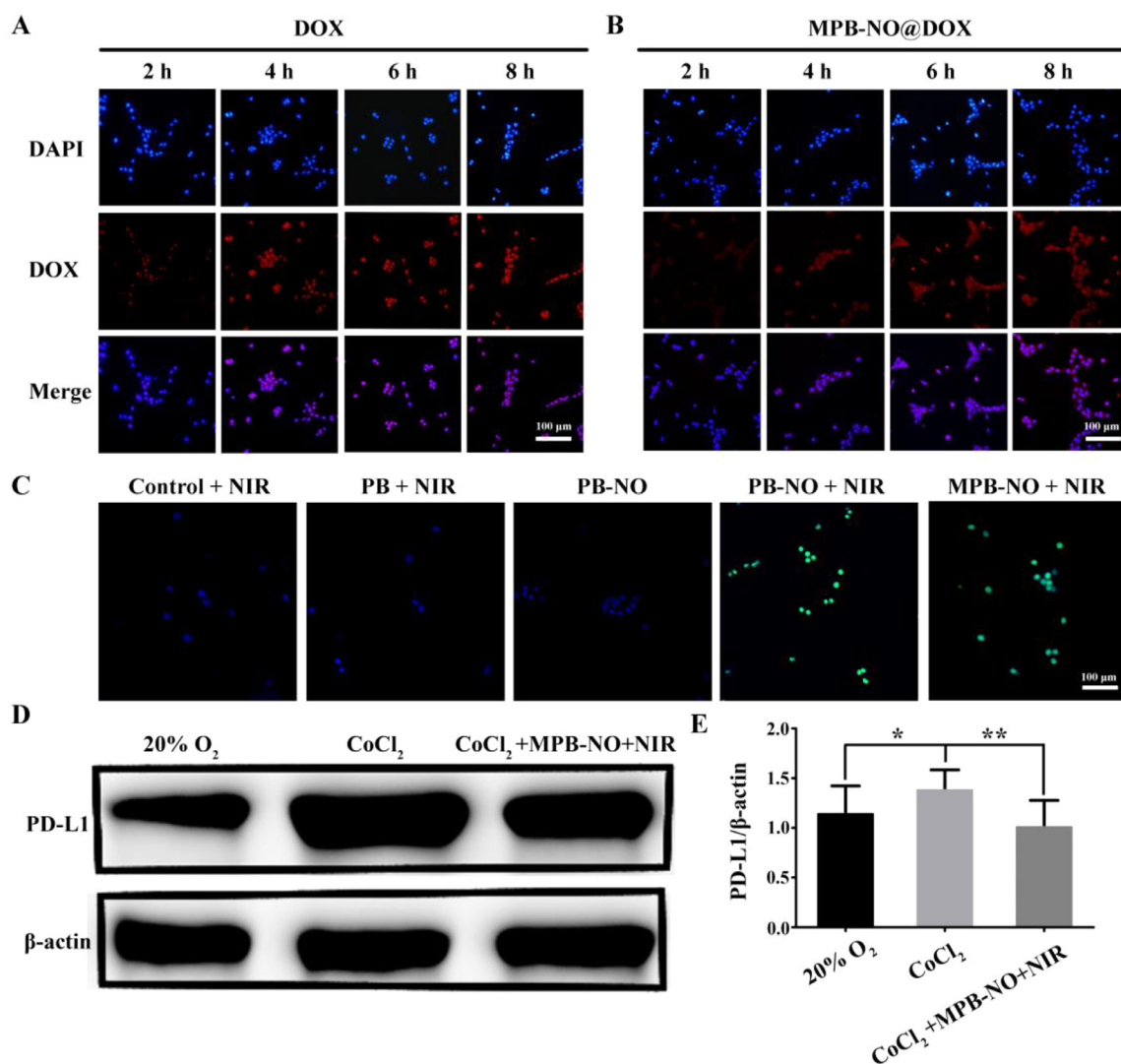


Fig. 3 – Cellular uptake, NO release, and PD-L1 expression. Cellular uptake of (A) DOX (2 µg/ml) and (B) MPB-NO@DOX (2 µg/ml DOX) by 4T1 cells. The scale bars are 100 µm. (C) Fluorescence microscope images showing NO release from PB, PB-NO, and MPB-NO in 4T1 cells. The scale bar is 100 µm. (D) and (E) PD-L1 expression in 4T1 cells with different treatments. * $P < 0.05$ and ** $P < 0.01$.

the MPB-NO + 808 nm laser irradiation group than that in the CoCl₂ group, indicating that the NO released from MPB-NO upon 808 nm laser irradiation markedly reduced PD-L1 expression in the hypoxic cells.

3.6. Anti-tumor activity of ATRA in vitro

It is crucial to adjust the ratio of M1- to M2-type TAM to improve the tumor immune microenvironment for enhancing the efficacy of cancer therapy [66]. Therefore, the effect of ATRA on TAM polarization was examined. As indicated in Fig. 4A, the proportion of M1-type TAM in the control group (ATRA = 0 µM) was 44.1%, while that in the ATRA (0.25–5 µM) group increased to 56.4%–66.8%, and the proportion of M1 increased gradually with the increase in ATRA concentration. These results suggested that ATRA inhibited the polarization

of RAW 264.7 cells to M2-type TAM. Next, we induced RAW 264.7 cells to polarize into M2-type macrophages with IL-4 and then cultured them with ATRA at different concentrations. Finally, the proportion of M1-type cells was determined using flow cytometry. As manifested in Fig. 4B, the proportion of M1-type in the control group (ATRA = 0 µM) was 33.3% and increased to 40.9%–56.9% with the increase in ATRA concentration, suggesting that ATRA could reverse some M2-type macrophages into the M1-type.

ATRA has been reported to effectively inhibit tumor cell migration. In this study, the inhibition of 4T1 cell metastasis by ATRA was investigated. ATRA significantly inhibited 4T1 migration at 0.25 µM, and its inhibitory effect slightly increased with increased concentration (Fig. 4C and D). These results confirm that ATRA effectively inhibited 4T1 cell migration at 0.25–5 µM.

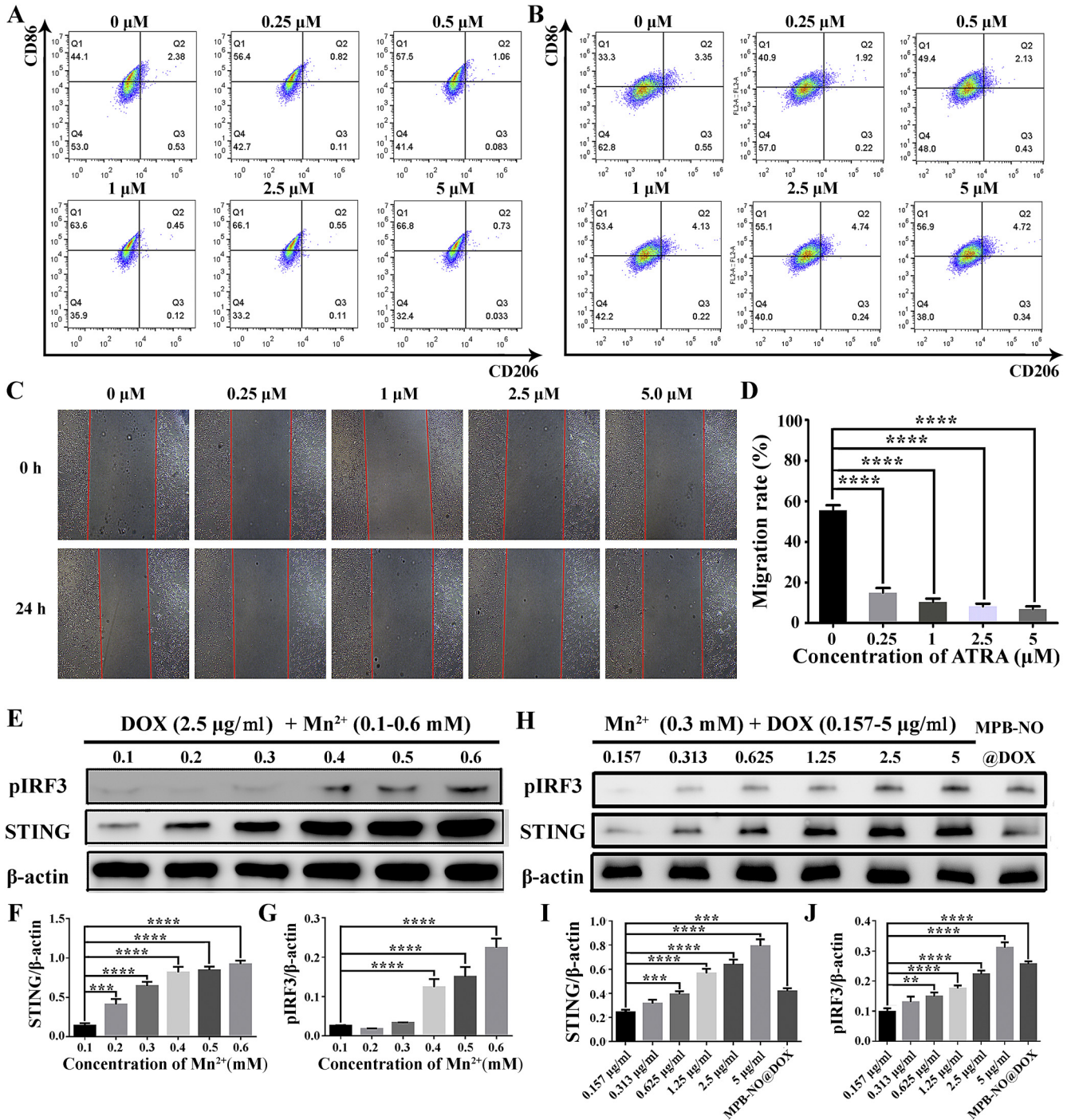


Fig. 4 – Study on immune-activation ability of the MPB-NO@DOX + ATRA gel. (A) ATRA promoted the polarization of RAW 264.7 to M1-type macrophages *in vitro*. RAW 264.7 macrophages were incubated in a cell medium containing IL-4 (40 ng/ml) and ATRA (0, 0.25, 0.5, 1, 2.5, and 5 μM) for 36 h, followed by the addition of the PE-CD86 antibody and FITC-CD206 antibody. **(B)** ATRA reversed M2-type into M1-type macrophages *in vitro*. RAW 264.7 macrophages were first polarized into M2-type by incubation with IL-4 at 37 °C for 36 h, followed by incubation with ATRA (0, 0.25, 0.5, 1, 2.5, and 5 μM) and the addition of the PE-CD86 antibody and FITC-CD206 antibody. **(C)** Photos depicting the inhibition of ATRA at different concentrations (0, 0.25, 1, 2.5, and 5 μM) on the migration of 4T1 cells. **(D)** Quantitative analysis of the effect of the inhibition of ATRA on migration of 4T1 cells. **(E)** Western blotting photos demonstrating the expression of STING and pIRF3 in the cells co-cultured with DOX at 2.5 μg/ml and Mn²⁺ at the concentrations of 0.1, 0.2, 0.3, 0.4, 0.5, and 0.6 mM, respectively. **(F)** Quantitative analysis of STING expression. **(G)** Quantitative analysis of pIRF3 expression. **(H)** Western blotting photos demonstrating the expression of STING and pIRF3 in the cells co-cultured with DOX at concentrations of 0.157, 0.313, 0.625, 1.25, 2.5, and 5 μg/ml, Mn²⁺ at 0.3 mM and MPB-NO@DOX, respectively. **(I)** Quantitative analysis of STING expression. **(J)** Quantitative analysis of pIRF3 expression. **P < 0.01, ***P < 0.001, and ****P < 0.0001.

3.7. cGAS-STING pathway was activated in vitro

Mn²⁺ and dsDNA can promote the synthesis of cGAMP, which acts as a paracrine stimulator of antigen-presenting cells (APC) and activates the downstream protein STING in dendritic cells (DCs), thereby producing a large amount of IFN-I. The expression of STING protein in 4T1 cells was significantly increased after the 4T1 cells were treated with MPB-NO@DOX and co-cultured with DCs (Fig. S10). This may be due to the activation of the STING pathway in DCs. Based on extant literature, we speculated that the degree of activation of the cGAS-STING pathway was positively correlated with dsDNA and Mn²⁺ concentrations. Thus, we further investigated the optimal ratio of DOX to Mn²⁺ for activating the cGAS-STING pathway. It was found that the expressions of STING and pIRF3 proteins increased with the increase in Mn²⁺ concentration from 0.1 to 0.6 mM at 2.5 µg/ml DOX concentration (Fig. 4E-4G). Noteworthy, the cells began to undergo apoptosis when the Mn²⁺ concentration was increased to 0.4 mM. Therefore, 0.3 mM Mn²⁺ was used to optimize the DOX concentration to activate the cGAS-STING pathway *in vitro*. The expression of STING and pIRF3 proteins increased with the increase in DOX concentration from 0.157 to 5 µg/ml when the Mn²⁺ concentration was 0.3 mM (Fig. 4H-4J). The expression of STING and pIRF3 proteins at DOX concentrations of 2.5 and 5 µg/ml was up-regulated. Considering the toxicity of DOX, 2.5 µg/ml was determined to be the optimal DOX concentration. Mn²⁺ at 0.3 mM and DOX at 2.5 µg/ml were the optimal combinations, which could be achieved by regulating the loading efficacy of DOX in MPB-NO@DOX.

3.8. Prevention of postoperative tumor recurrence

To investigate the photothermal conversion effect of MPB-NO *in vivo*, temperature changes at the postoperative tumor site were investigated. The local temperature at the tumor site of the mice treated with MPB-NO-loaded gels increased from 29.5 to 51.0 °C after irradiation for 3 min, while there was little change in the NS-loaded gel group (Fig. 2H). These results confirmed that MPB-NO had a high photothermal conversion effect *in vivo*.

Subcutaneous 4T1 tumor-bearing and post-surgical mice were randomly divided into eight groups (n = 6): (a) NS gel group, (b) PB gel group, (c) MPB-NO gel group, (d) MPB-NO gel + NIR group, (e) MPB-NO@DOX gel group, (f) MPB-NO@DOX gel + NIR group, (g) MPB-NO@DOX + ATRA gel group and (h) MPB-NO@DOX + ATRA gel + NIR group (Figs. 5A and S11). The weight and size of the tumors in MPB-NO gel and MPB-NO gel + NIR groups were slightly smaller than in NS gel and PB gel groups, which could be attributed to the weak ability of Mn²⁺ alone to activate the cGAS-STING pathway (Fig. 5B-5D). The weight and size of the tumors in the MPB-NO@DOX gel + NIR group were smaller than those in the MPB-NO@DOX gel group, which might be because the released NO from the MPB-NO@DOX gel after irradiation reduced the expression of PD-L1, enabling lymphotoxin-producing T cells to play a more effective immune-killing role in tumor cells. The MPB-NO@DOX + ATRA gel + NIR group exhibited the lowest tumor recurrence rate and the smallest tumor volume. As

disclosed in Fig. 5E, the tumor recurrence rates in the groups of NS gel, PB gel, MPB-NO gel, and MPB-NO gel + NIR were 100% and the tumor volume of the first two groups reached about 1,000–1,500 mm³ after treatment, indicating that the inhibitory effect of the MPB-NO gel on the prevention of postoperative tumor recurrence was negligible. TdT-mediated dUTP nick end labeling (TUNEL) and hematoxylin and eosin (H&E) staining were performed on the tumors in each group after treatments. The results demonstrated that the tumor cells grew well with compact structure in the NS gel and PB gel groups, followed by MPB-NO gel and MPB-NO gel + NIR groups, whereas those in other groups were affected to varying degrees, consistent with the change in the tumor volume (Fig. 5F).

3.9. Prevention of post-surgical tumor recurrence by modulating the tumor immune microenvironment

Because the spleen is an important immune organ in the body, we first determined the spleen index. The spleen indices in the NS gel, PB gel, MPB-NO gel, and MPB-NO gel + NIR groups were much lower than those in the MPB-NO@DOX gel, MPB-NO@DOX gel + NIR, MPB-NO@DOX + ATRA gel, and MPB-NO@DOX + ATRA gel + NIR groups (Fig. S12). This provided a preliminary indication that the combination of Mn²⁺ and DOX could effectively activate the immune system, producing a strong anti-tumor recurrence immune response.

Subsequently, we euthanized the treated mice and used flow cytometry to determine the proportion of each type of immune cell (Fig. 6A-6D). The percentage of DCs increased significantly after treatment with the MPB-NO@DOX gel, MPB-NO@DOX gel + NIR, MPB-NO@DOX + ATRA gel, and MPB-NO@DOX + ATRA gel + NIR (Fig. S13). The proportion of M1-type macrophages increased to some extent and the proportion of M2-type macrophages decreased to different degrees after treatment with the MPB-NO@DOX gel, MPB-NO@DOX gel + NIR, MPB-NO@DOX + ATRA gel, and MPB-NO@DOX + ATRA gel + NIR (Fig. S14 and S15). Higher proportions of M1-type macrophages were found in the MPB-NO@DOX + ATRA gel and MPB-NO@DOX NPs + ATRA gel + NIR groups than in the other groups, indicating that the CAT-like activity of PB combined with ATRA had a good synergistic effect in promoting the transition of TAM to M1-type macrophages. The proportion of M1-type macrophages in the groups treated with NIR laser irradiation was slightly higher than that in the untreated groups, suggesting that NO released after laser irradiation may affect TAM polarization. These results were further verified by immunofluorescence staining of tumor tissue sections from mice treated with different gels (Fig. S16). More importantly, the ratio of M1-type macrophages to M2-type macrophages within the TME was significantly enhanced after gel treatment, revealing that the gel encapsulating MPB-NO@DOX and ATRA exerted a positive effect on TAM polarization (Fig. S17). In addition, the infiltration of CD8⁺T cells and the percentage of mature DCs were significantly increased in the MPB-NO@DOX gel, MPB-NO@DOX gel + NIR, MPB-NO@DOX + ATRA gel and MPB-NO@DOX + ATRA gel + NIR groups (Fig. S18). These results demonstrated that the gel encapsulating MPB-NO@DOX and ATRA could pre-program the immunosuppressive TME. This

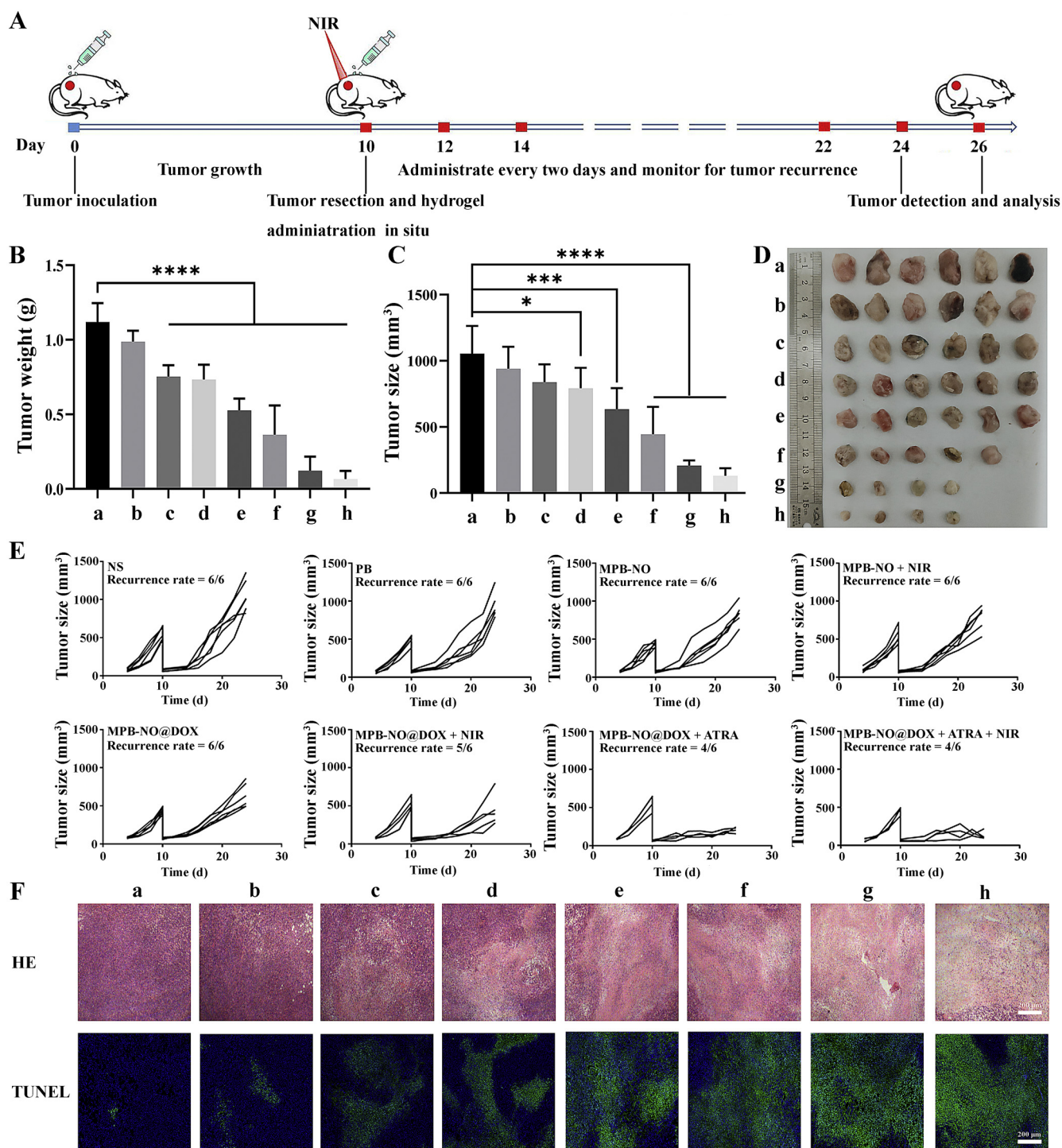


Fig. 5 – Prevention of Postoperative Tumor Recurrence. (A) Schematic illustration of the therapeutic gel therapy in a mouse model of incomplete tumor resection. The tumor was resected, and fibrin gel was implanted in situ. (B) The tumor weight of each group of mice after different treatments. **** $P < 0.0001$, significantly different. (C) The tumor size of each group of mice after different treatments. * $P < 0.05$, *** $P < 0.001$, and **** $P < 0.0001$, significantly different. (D) Photos of the excised tumors at the therapeutic endpoint. (E) Individual tumor growth kinetics in each group during the treatments. (F) H&E- and TUNEL-stained sections of tumor tissues of mice in each group. The scale bars are 200 μm . Data are presented as mean \pm S.D. ($n = 6$).

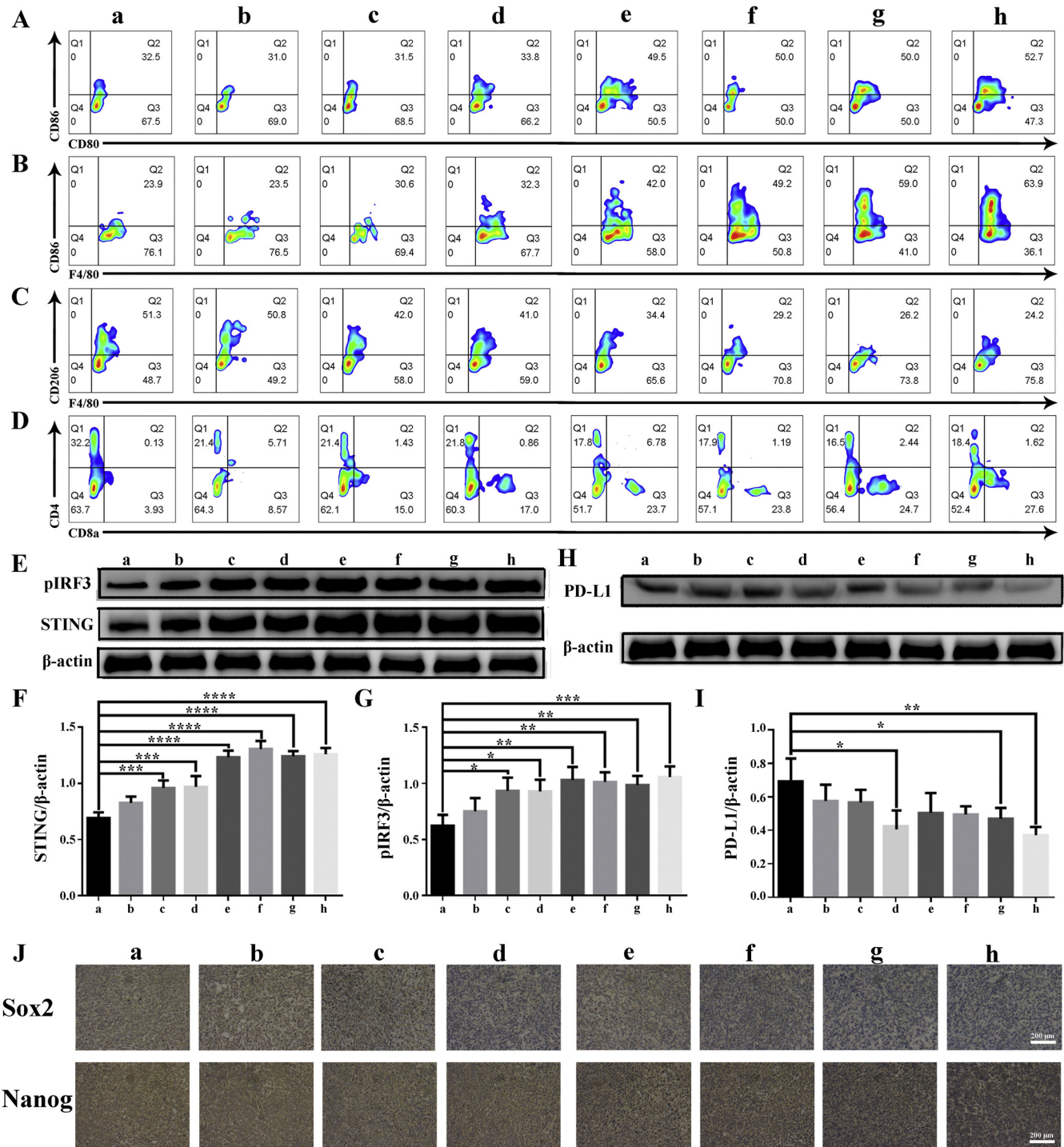


Fig. 6 – Immune responses of the gels *in vivo*. Flow cytometric analysis of (A) dendritic cells (DCs, CD86⁺CD80⁺), (B) M1-type macrophages (F4/80⁺CD86⁺), (C) M2-type macrophages (F4/80⁺CD206⁺), and (D) CD4⁺ and CD8⁺ T cells in tumor tissues of each group with different treatments. (E) Western blotting showing the expressions of STING and pIRF3 in tumor tissues of each group with different treatments. (F) Quantitative analysis of STING expression. (G) Quantitative analysis of pIRF3 expression. (H) Western blotting showing PD-L1 expression in tumor tissues of each group with different treatments. (I) Quantitative analysis of PD-L1 expression. (J) Immunohistochemical images of CSCs in tumor tissue after different treatments. The scale bar is 200 μm. Data are presented as mean ± SD (n = 6, *P < 0.05, **P < 0.01, ***P < 0.001, and ****P < 0.0001).

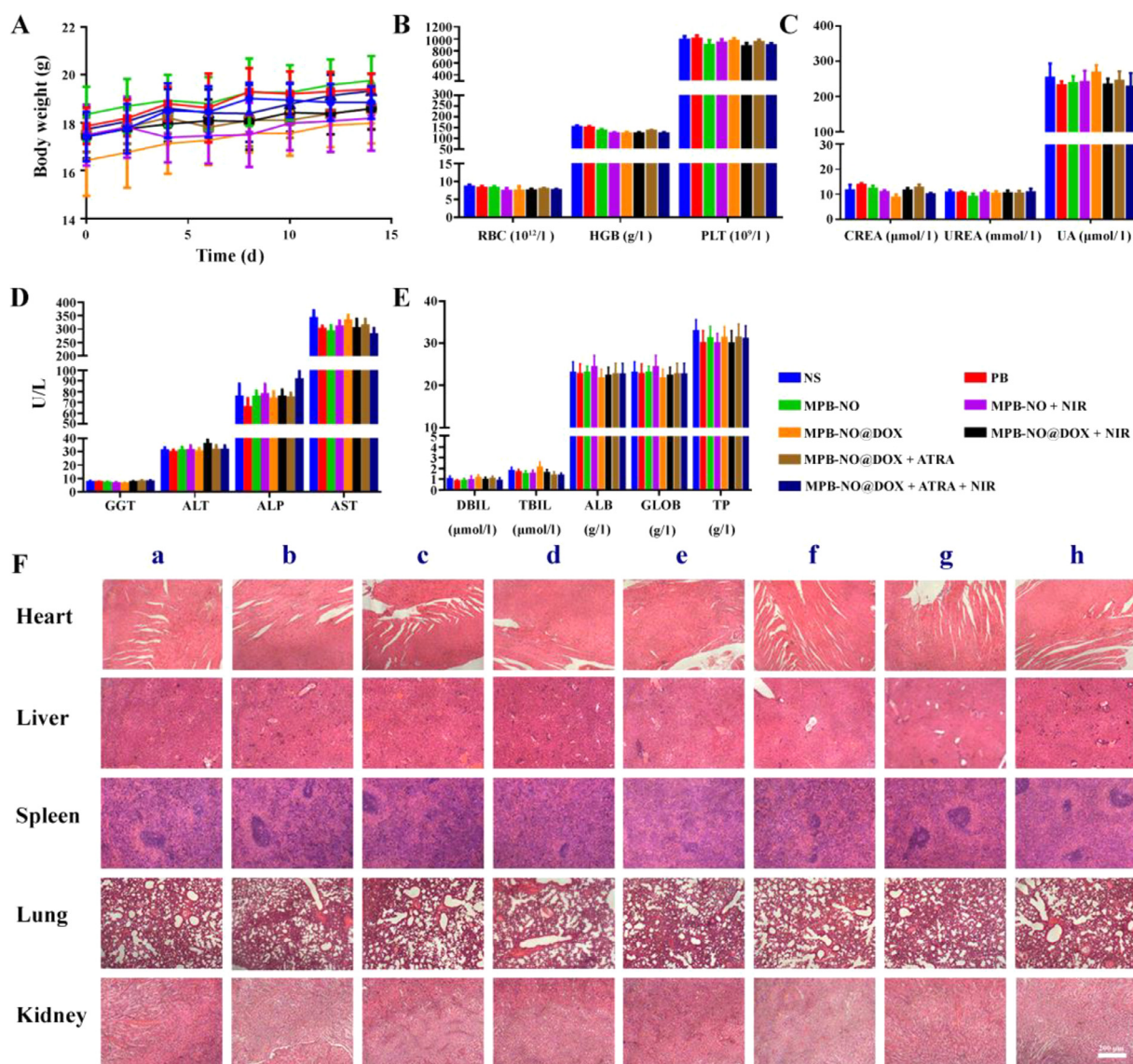


Fig. 7 – Biosafety studies. (A) Changes in body weight of mice during treatment. (B) Routine blood test of mice in each group. (C, D). Liver function test of mice in each group. (E) Renal function test of mice in each group. (F) H&E staining sections of major organs of mice in each group. The scale bar is 200 μm . Data are presented as mean \pm SD ($n = 6$).

was because the combination of Mn^{2+} and DOX significantly activated the cGAS-STING pathway, thereby enhancing the activation and function of immune cells. This was further confirmed by the expressions of STING and pIRF3 in the tumor tissues of mice subjected to different treatments (Fig. 6E-6G). The DOX released from the MPB-NO@DOX + ATRA gel disrupted DNA, and the Mn^{2+} released from the gel accelerated the recognition of dsDNA by cGAS to activate the immune response against post-surgical tumor recurrence *in vivo*. We further measured the expression level of PD-L1 by western blotting. As illustrated in Fig. 6H and 6I, PD-L1 expression was lower in MPB-NO gel + NIR and MPB-NO@DOX + ATRA gel + NIR groups than in the other groups. This might be because PB and MPB-NO exhibited CAT-like activity, and MnO_2 underwent a redox

reaction with H_2O_2 , which alleviated the hypoxic TME and downregulated PD-L1 expression. PD-L1 expression in the groups with NIR laser irradiation was much lower than that in the groups without irradiation because 808 nm laser irradiation resulted in the breakage of PB-NO and triggered the release of NO. In turn, it has been reported that NO can reduce HIF- α expression, thereby further reducing PD-L1 expression [65].

Inspired by the anti-tumor activity of ATRA *in vitro* and its ability to differentiate CSCs to tumor cells, we evaluated common indicators of cell stemness *in vivo*. The expressions of Sox2 and Nanog in the groups containing ATRA were significantly lower than those in the other groups without ATRA, confirming that ATRA strongly reduced stemness *in vivo* (Fig. 6).

3.10. Biosafety in vivo

The toxicity of MPB-NO@DOX + ATRA gel in mice was also investigated. No significant difference was observed in the body weight among the different treatment groups, suggesting that the MPB-NO@DOX + ATRA gel was nontoxic (Fig. 7A). Routine blood results revealed no obvious differences in the red blood cells, hemoglobin, and platelets of the mice in each group (Fig. 7B). As displayed in Fig. 7C-7E, the renal and liver functions of the mice in each group were normal. In addition, H&E staining demonstrated that the heart, liver, lung, kidney, and spleen in all treatment groups were in good condition without any pathological phenomena (Fig. 7F). These results revealed that the MPB-NO@DOX + ATRA gel had good biocompatibility.

4. Conclusion

We successfully developed an injectable fibrin gel encapsulating a Mn²⁺/NO-based immune nano-activator (MPB-NO@DOX) and ATRA, which demonstrated sustained release and good biocompatibility. After MPB-NO@DOX NPs were uptaken by tumor cells, intracellular GSH and acidic TME triggered the release of Mn²⁺ and DOX. The fragmented DNA induced by the released DOX and Mn²⁺ synergistically activated the cGAS-STING pathway to promote the maturation of DCs, thus enhancing their ability to present tumor-specific antigens and promote the immune function of T cells. In addition, NO release triggered by NIR irradiation reduced the expression of PD-L1, thereby enhancing the immune-killing effect of T cells. Importantly, ATRA in the gel reduced the stemness of the tumor, allowing tumor cells to be recognized and killed by the immune cells. This combined effect ensured that the MPB-NO@DOX NPs + ATRA gel plus laser irradiation was effective in preventing postoperative tumor recurrence.

Conflicts of interest

The authors declare that they have no known competing financial interests or personal relationships that could have appeared to influence the work reported in this paper.

Acknowledgements

This study was supported by the National Natural Science Foundation of China (No. 82003298), the Scientific and Technological Project of Henan Province (No. 232102310392), the Key Research and Development Projects of Henan Province (No. 222102310453, 212102311025), Postdoctoral Research Grant in Henan Province (No. 201901025), the Key Research Project of Henan Higher Education Institutions (No. 18A350003), Open Fund of Key Laboratory of Targeting Therapy and Diagnosis for Critical Diseases, Henan Province (No. NMZL2020102), the Natural Science Foundation of Chongqing (No. cstc2019jcyj-msxmX0035), and the Scientific Research

Seedling Project of Chongqing Medicinal Biotechnology Association (No. cmba2022kyym-zkxmQ0009).

Supplementary materials

Supplementary material associated with this article can be found, in the online version, at doi:10.1016/j.ajps.2024.100901.

REFERENCES

- [1] Clough KB, Kaufman GJ, Nos C, Buccimazza I, Sarfati IM. Improving breast cancer surgery: a classification and quadrant per quadrant atlas for oncological surgery. *Ann Surg Oncol* 2010;17(5):1375–91.
- [2] Chen Z, Zhang P, Xu Y, Yan J, Liu Z, Lau WB, et al. Surgical stress and cancer progression: the twisted tango. *Mol Cancer* 2019;18:132.
- [3] Adesoye T, Irwin S, Sun SX, Lucci A, Teshome M. Contemporary surgical management of inflammatory breast cancer: a narrative review. *Chin Clin Oncol* 2021;10(6):57.
- [4] Turajlic S, Swanton C. Metastasis as an evolutionary process. *Science* 2016;352(6282):169–75.
- [5] Liu Y, Yeh C, Lin K. Cancer stem cell functions in hepatocellular carcinoma and comprehensive therapeutic strategies. *Cells* 2020;9(6).
- [6] Chen Q, Wang C, Zhang X, Chen G, Hu Q, Li H, et al. In situ sprayed bioresponsive immunotherapeutic gel for post-surgical cancer treatment. *Nat Nanotechnol* 2019;14(1):89–97.
- [7] Landskron G, De la Fuente M, Thuwajit P, Thuwajit C, Hermoso MA. Chronic inflammation and cytokines in the tumor microenvironment. *J Immunol Res* 2014;2014:149185.
- [8] Tohme S, Yazdani HO, Al-Khafaji AB, Chidi AP, Loughran P, Mowen K, et al. Neutrophil extracellular traps promote the development and progression of liver metastases after surgical stress. *Cancer Res* 2016;76(6):1367–80.
- [9] de Thé H. Differentiation therapy revisited. *Nat Rev Cancer* 2018;18(2):117–27.
- [10] Arima Y, Nobusue H, Saya H. Targeting of cancer stem cells by differentiation therapy. *Cancer Sci* 2020;111(8):2689–95.
- [11] Lewis AC, Kats LM. Non-genetic heterogeneity, altered cell fate and differentiation therapy. *Embo Mol Med* 2021;13(3):e12670.
- [12] Lim YC, Kang HJ, Kim YS, Choi EC. All-trans-retinoic acid inhibits growth of head and neck cancer stem cells by suppression of wnt/ β -catenin pathway. *Eur J Cancer* 2012;48(17):3310–18.
- [13] Nguyen PH, Giraud J, Staedel C, Chambonnier L, Dubus P, Chevreton E, et al. All-trans retinoic acid targets gastric cancer stem cells and inhibits patient-derived gastric carcinoma tumor growth. *Oncogene* 2016;35(43):5619–28.
- [14] Li Y, Atkinson K, Zhang T. Combination of chemotherapy and cancer stem cell targeting agents: preclinical and clinical studies. *Cancer Lett* 2017;396:103–9.
- [15] Zhou Q, Xian M, Xiang S, Xiang D, Shao X, Wang J, et al. All-trans retinoic acid prevents osteosarcoma metastasis by inhibiting m2 polarization of tumor-associated macrophages. *Cancer Immunol Res* 2017;5(7):547–59.
- [16] Shao X, Xiang S, Chen Y, Zhang N, Cao J, Zhu H, et al. Inhibition of m2-like macrophages by all-trans retinoic acid prevents cancer initiation and stemness in osteosarcoma cells. *Acta Pharmacol Sin* 2019;40(10):1343–50.
- [17] Sun R, Liu Y, Li S, Shen S, Du X, Xu C, et al. Co-delivery of all-trans-retinoic acid and doxorubicin for cancer therapy with synergistic inhibition of cancer stem cells. *Biomaterials* 2015;37:405–14.

- [18] Liu Y, Yu F, Dai S, Meng T, Zhu Y, Qiu G, et al. All-trans retinoic acid and doxorubicin delivery by folic acid modified polymeric micelles for the modulation of pin1-mediated dox-induced breast cancer stemness and metastasis. *Mol Pharm* 2021;18(11):3966–78.
- [19] Shen S, Xu X, Lin S, Zhang Y, Liu H, Zhang C, et al. A nanotherapeutic strategy to overcome chemotherapeutic resistance of cancer stem-like cells. *Nat Nanotechnol* 2021;16(1):104–13.
- [20] Pan C, Liu H, Robins E, Song W, Liu D, Li Z, et al. Next-generation immuno-oncology agents: current momentum shifts in cancer immunotherapy. *J Hematol Oncol* 2020;13(1):29.
- [21] Riley RS, June CH, Langer R, Mitchell MJ. Delivery technologies for cancer immunotherapy. *Nat Rev Drug Discov* 2019;18(3):175–96.
- [22] Xu J, Lv J, Zhuang Q, Yang Z, Cao Z, Xu L, et al. A general strategy towards personalized nanovaccines based on fluoropolymers for post-surgical cancer immunotherapy. *Nat Nanotechnol* 2020;15(12):1043–52.
- [23] Velcheti V, Schalper K. Basic overview of current immunotherapy approaches in cancer. American society of clinical oncology educational book. American Society of Clinical Oncology. Annual Meeting 2016;35:298–308.
- [24] Kubli SP, Berger T, Araujo DV, Siu LL, Mak TW. Beyond immune checkpoint blockade: emerging immunological strategies. *Nat Rev Drug Discov* 2021;20(12):899–919.
- [25] Zhu S, Zhang T, Zheng L, Liu H, Song W, Liu D, et al. Combination strategies to maximize the benefits of cancer immunotherapy. *J Hematol Oncol* 2021;14(1):156.
- [26] Wang C, Sun W, Ye Y, Hu Q, Bomba H, Gu Z. *in situ* activation of platelets with checkpoint inhibitors for post-surgical cancer immunotherapy. *Nat Biomed Eng* 2017;1(2).
- [27] Hu Q, Li H, Archibong E, Chen Q, Ruan H, Ahn S, et al. Inhibition of post-surgery tumour recurrence via a hydrogel releasing car-t cells and anti-pdl1-conjugated platelets. *Nat Biomed Eng* 2021;5(9):1038–47.
- [28] Li Z, Ding Y, Liu J, Wang J, Mo F, Wang Y, et al. Depletion of tumor associated macrophages enhances local and systemic platelet-mediated anti-pd-1 delivery for post-surgery tumor recurrence treatment. *Nat Commun* 2022;13(1):1845.
- [29] Jiang M, Chen P, Wang L, Li W, Chen B, Liu Y, et al. cGAS-STING, an important pathway in cancer immunotherapy. *J Hematol Oncol* 2020;13(1):81.
- [30] Hopfner K, Hornung V. Molecular mechanisms and cellular functions of cGAS-STING signalling. *Nat Rev Mol Cell Biol* 2020;21(9):501–21.
- [31] Gan Y, Li X, Han S, Liang Q, Ma X, Rong P, et al. The cgas/sting pathway: a novel target for cancer therapy. *Front Immunol* 2021;12:795401.
- [32] Du H, Xu T, Cui M. cGAS-STING signaling in cancer immunity and immunotherapy. *Biomed Pharmacother* 2021;133:110972.
- [33] Lv M, Chen M, Zhang R, Zhang W, Wang C, Zhang Y, et al. Manganese is critical for antitumor immune responses via cGAS-STING and improves the efficacy of clinical immunotherapy. *Cell Res* 2020;30(11):966–79.
- [34] Wang C, Sun Z, Zhao C, Zhang Z, Wang H, Liu Y, et al. Maintaining manganese in tumor to activate cGAS-STING pathway evokes a robust abscopal anti-tumor effect. *J Control Release* 2021;331:480–90.
- [35] Wang C, Guan Y, Lv M, Zhang R, Guo Z, Wei X, et al. Manganese increases the sensitivity of the cGAS-STING pathway for double-stranded DNA and is required for the host defense against DNA viruses. *Immunity* 2018;48(4):675–87.
- [36] Wen Y, Liu Y, Chen C, Chi J, Zhong L, Zhao Y, et al. Metformin loaded porous particles with bio-microenvironment responsiveness for promoting tumor immunotherapy. *Biomater Sci* 2021;9(6):2082–9.
- [37] Murphy DA, Cheng H, Yang T, Yan X, Adjei IM. Reversing hypoxia with plga-encapsulated manganese dioxide nanoparticles improves natural killer cell response to tumor spheroids. *Mol Pharm* 2021;18(8):2935–46.
- [38] Sun X, Zhang Y, Li J, Park KS, Han K, Zhou X, et al. Amplifying sting activation by cyclic dinucleotide-manganese particles for local and systemic cancer metalloimmunotherapy. *Nat Nanotechnol* 2021;16(11):1260–70.
- [39] Zhang K, Qi C, Cai K. Manganese-based tumor immunotherapy. *Adv Mater* 2023;35(19):e2205409.
- [40] Huang X, Zhong Y, Li Y, Zhou X, Yang L, Zhao B, et al. Black phosphorus-synergic nitric oxide nanogasholder spatiotemporally regulates tumor microenvironments for self-amplifying immunotherapy. *ACS Appl Mater Interfaces* 2022;14(33):37466–77.
- [41] Kim J, Francis DM, Sestito LF, Archer PA, Manspeaker MP, O'Melia MJ, et al. Thermosensitive hydrogel releasing nitric oxide donor and anti-ctla-4 micelles for anti-tumor immunotherapy. *Nat Commun* 2022;13(1):1479.
- [42] Yang Z, Gao D, Guo X, Jin L, Zheng J, Wang Y, et al. Fighting immune cold and reprogramming immunosuppressive tumor microenvironment with red blood cell membrane-camouflaged nanobullets. *ACS Nano* 2020;14(12):17442–57.
- [43] Jiang W, Dong W, Li M, Guo Z, Wang Q, Liu Y, et al. Nitric oxide induces immunogenic cell death and potentiates cancer immunotherapy. *ACS Nano* 2022;16(3):3881–94.
- [44] Hu Q, Shi J, Zhang J, Wang Y, Guo Y, Zhang Z. Progress and prospects of regulatory functions mediated by nitric oxide on immunity and immunotherapy. *Adv Ther* 2021;4(8):2100032.
- [45] Yang Y, Huang Z, Li L. Advanced nitric oxide donors: chemical structure of no drugs, no nanomedicines and biomedical applications. *Nanoscale* 2021;13(2):444–59.
- [46] Kim J, Thomas SN. Opportunities for nitric oxide in potentiating cancer immunotherapy. *Pharmacol Rev* 2022;74(4):1146–75.
- [47] Park CG, Hartl CA, Schmid D, Carmona EM, Kim H, Goldberg MS. Extended release of perioperative immunotherapy prevents tumor recurrence and eliminates metastases. *Sci Transl Med* 2018;10(433).
- [48] Leng Q, Li Y, Zhou P, Xiong K, Lu Y, Cui Y, et al. Injectable hydrogel loaded with paclitaxel and epirubicin to prevent postoperative recurrence and metastasis of breast cancer. *Mater Sci Eng C* 2021;129:112390.
- [49] Bastiancich C, Bianco J, Vanvarenberg K, Ucarar B, Joudiou N, Gallez B, et al. Injectable nanomedicine hydrogel for local chemotherapy of glioblastoma after surgical resection. *J Control Release* 2017;264:45–54.
- [50] Chen S, Qiu Q, Wang D, She D, Yin B, Gu G, et al. Dual-sensitive drug-loaded hydrogel system for local inhibition of post-surgical glioma recurrence. *J Control Release* 2022;349:565–79.
- [51] Bu L, Yan J, Wang Z, Ruan H, Chen Q, Gunadhi V, et al. Advances in drug delivery for post-surgical cancer treatment. *Biomaterials* 2019;219:119182.
- [52] Zhuang B, Chen T, Xiao Z, Jin Y. Drug-loaded implantable surgical cavity-adaptive hydrogels for prevention of local tumor recurrence. *Int J Pharm* 2020;577:119048.
- [53] Qian Q, Wang D, Shi L, Zhang Z, Qian J, Shen J, et al. A pure molecular drug hydrogel for post-surgical cancer treatment. *Biomaterials* 2021;265:120403.
- [54] Tang R, Liu Z, Gu S, Liu X. Multiple local therapeutics based on nano-hydrogel composites in breast cancer treatment. *J Mater Chem B* 2021;9(6):1521–35.
- [55] Ogunnaike EA, Valdivia A, Yazdimaghani M, Leon E, Nandi S, Hudson H, et al. Fibrin gel enhances the antitumor effects of chimeric antigen receptor t cells in glioblastoma. *Sci Adv* 2021;7(41):g5841.

- [56] Chao Y, Wei T, Li Q, Liu B, Hao Y, Chen M, et al. Metformin-containing hydrogel scaffold to augment cart therapy against post-surgical solid tumors. *Biomaterials* 2023;295:122052.
- [57] Mohammadi M, Karimi M, Malaek-Nikouei B, Torkashvand M, Alibolandi M. Hybrid in situ-forming injectable hydrogels for local cancer therapy. *Int J Pharm* 2022;616:121534.
- [58] Zhang L, Zhou J, Hu L, Han X, Zou X, Chen Q, et al. In situ formed fibrin scaffold with cyclophosphamide to synergize with immune checkpoint blockade for inhibition of cancer recurrence after surgery. *Adv Funct Mater* 2020;30(7):1906922.
- [59] Zheng D, Hong S, Zhang Q, Dong X, Pan P, Song W, et al. Controllable gelation of artificial extracellular matrix for altering mass transport and improving cancer therapies. *Nat Commun* 2020;11(1):4907.
- [60] Li C, Wan Y, Zhang Y, Fu L, Blum NT, Cui R, et al. In situ sprayed starvation/chemodynamic therapeutic gel for post-surgical treatment of idh1 (r132h) glioma. *Adv Mater* 2022;34(5):e2103980.
- [61] Feng T, Wan J, Li P, Ran H, Chen H, Wang Z, et al. A novel nir-controlled no release of sodium nitroprusside-doped prussian blue nanoparticle for synergistic tumor treatment. *Biomaterials* 2019;214:119213.
- [62] Liu J, Zhao Z, Qiu N, Zhou Q, Wang G, Jiang H, et al. Co-delivery of iox1 and doxorubicin for antibody-independent cancer chemo-immunotherapy. *Nat Commun* 2021;12(1):2425.
- [63] Qi J, Jin F, You Y, Du Y, Liu D, Xu X, et al. Synergistic effect of tumor chemo-immunotherapy induced by leukocyte-hitchhiking thermal-sensitive micelles. *Nat Commun* 2021;12(1):4755.
- [64] Xiong X, Zhao J, Su R, Liu C, Guo X, Zhou S. Double enhancement of immunogenic cell death and antigen presentation for cancer immunotherapy. *Nano Today* 2021;39:101225.
- [65] Sung Y, Jin P, Chu L, Hsu F, Wang M, Chang C, et al. Delivery of nitric oxide with a nanocarrier promotes tumour vessel normalization and potentiates anti-cancer therapies. *Nat Nanotechnol* 2019;14(12):1160–9.
- [66] Cassetta L, Pollard JW. Targeting macrophages: therapeutic approaches in cancer. *Nat Rev Drug Discov* 2018;17(12):887–904.